Ultramicroscopy 126 (2013) 23–32

Contents lists available at SciVerse ScienceDirect

Ultramicroscopy

journal homepage: www.elsevier.com/locate/ultramic

First experimental proof for aberration correction in XPEEM: Resolution, transmission enhancement, and limitation by space charge effects

Th. Schmidt [a,*], A. Sala [a], H. Marchetto [a], E. Umbach [b], H.-J. Freund [a]

[a] Fritz Haber Institute of the Max Planck Society, Department of Chemical Physics, Faradayweg 4-6, D-14195 Berlin, Germany
[b] Karlsruhe Institute of Technology, 76021 Karlsruhe, Germany

ARTICLE INFO

Article history:
Received 17 August 2012
Received in revised form
9 November 2012
Accepted 13 November 2012
Available online 23 November 2012

Keywords:
Aberration correction
Space charge
X-ray induced photoelectron emission microscopy
Low energy electron microscopy
Transmission
Lateral resolution

ABSTRACT

The positive effect of double aberration correction in x-ray induced Photoelectron Emission Microscopy (XPEEM) has been successfully demonstrated for both, the lateral resolution and the transmission, using the Au 4f XPS peak for element specific imaging at a kinetic energy of 113 eV. The lateral resolution is improved by a factor of four, compared to a non-corrected system, whereas the transmission is enhanced by a factor of 5 at a moderate resolution of 80 nm. With an optimized system setting, a lateral resolution of 18 nm could be achieved, which is up to now the best value reported for energy filtered XPEEM imaging. However, the absolute resolution does not yet reach the theoretical limit of 2 nm, which is due to space charge limitation. This occurs along the entire optical axis up to the contrast aperture. In XPEEM the pulsed time structure of the exciting soft x-ray light source causes a short and highly intense electron pulse, which results in an image blurring. In contrast, the imaging with elastically reflected electrons in the low energy electron microscopy (LEEM) mode yields a resolution clearly below 5 nm. Technical solutions to reduce the space charge effect in an aberration-corrected spectro-microscope are discussed.

1. Introduction

Electron microscopes play an important role in fields of science where information on individual constituents of an ensemble is of interest. A typical example is catalysis, where the activity in a chemical reaction strongly depends on particular particle sizes and shapes. Hence it would be extremely useful to be able to investigate individual particles one by one to identify unique structure–reactivity relations. In order to reach this goal, a microscope has to provide a lateral resolution in the nanometer range and provide at the same time spectroscopic information that allows for chemical analysis and its correlation with electronic structure. Simultaneously, it is advantageous to increase the transmission to perform time dependent measurements such as growth and phase transition studies and, also, to reduce or avoid beam damage, as high transmission allows using more emitted electrons to increase the image intensity and reduce the acquisition time. A successful way to increase transmission and resolution at the same time in electron microscopy is to develop microscopes with aberration correction. Aberration correction has been successfully implemented in transmission electron microscopes (TEM) [1–3], scanning electron microscopes (SEM) [4], ultra-violet photo electron emission microscopy (UV-PEEM) [5] and low energy electron microscopes (LEEM) [6–9]. In the present contribution we focus on energy filtered x-ray-photo electron emission microscopy (XPEEM) with aberration correction. At synchrotron light sources there are only two systems available that use different concepts of energy filtering. [10] We use the so-called SMART (Spectromicroscopy with aberration correction for many relevant techniques) set-up at BESSY [11–13]. For highest resolution LEEM and XPEEM both, simultaneous spherical and chromatic aberration correction is needed. In the SMART a tetrode electron mirror integrated into the electron optics via a non dispersive magnetic deflection system is used for that purpose. So far, optimization has resulted in 2.6 nm resolution for the LEEM mode using a conservative definition of resolution; the optimization procedure has been published elsewhere [6]. A second procedure has recently been published by the Tromp group [14] using as well a tetrode electron mirror. In the case of the aberration corrected UV-PEEM in Portland [5], which is based upon the pioneering development of Gertrude Rempfer [15], a grid is inserted in the electron beam to visualize the aberration by the specific distortion of the projected image. This instrument demonstrated a resolution of 5.4 nm, the best achieved in UV-PEEM, by applying is a hyperbolic diode electron mirror as an aberration corrector. Using a diode instead of a tetrode mirror is sufficient in the UV-PEEM, because at the sample surface the initial kinetic energy of the emitted electrons is small (below 1 eV) and has a narrow distribution (below 1 eV). As a consequence, the

* Corresponding author. Tel.: +49 30 80621 4671; fax: +49 30 8413 4101.
E-mail address: schmidtt@fhi-berlin.mpg.de (Th. Schmidt).

0304-3991/$ - see front matter © 2012 Elsevier B.V. All rights reserved.
http://dx.doi.org/10.1016/j.ultramic.2012.11.004

diode mirror design is optimized for this specific situation of quasi fixed electron energy. In contrast to this, the kinetic energy of the emitted electrons in XPEEM are varied in an energy range between 0 eV and about 200 eV, to generate locally resolved x-ray photoemission spectra (XPS). Varying the energy, the spherical and chromatic aberrations of the objective lens change substantially by a factor of up to 10. Consequently, the aberration correction has to be tuned when the energy is changed. This is only possible with a tetrode mirror, which allows to independently vary the spherical and chromatic aberration over a wide range by changing three voltages. In order to perform XPEEM measurements an energy filter has to be integrated into the imaging optics [16]. An energy resolution of $\Delta E = 0.5$ eV or better is needed in the imaging mode. This calls for mechanical and electronic stability, i.e. high accuracy of the mechanical construction, perfect optical alignment, and correct and stable lens and mirror settings. Aberration correction is applied up to 3rd order. An important additional factor, which is the central topic of this contribution, is the limitation of spatial and energy resolution by space charge effects. This is a particular problem encountered when synchrotron light sources are being used to stimulate electron emission, as shown by Locatelli et al. [17,18] for an energy-filtered LEEM-PEEM system without aberration correction.

Space charge phenomena have been broadly studied for electron sources [19]. The so-called Boersch-effect [20] broadens the energy distribution, whereas the trajectory displacement effect, first investigated by Loeffer [21], limits the sharpness of electron source images in cathode lenses. An overview of the theoretical description of space charge and statistical Coulomb effects is given by Kruit and Jansen [21]. Space charge effects have also been observed in connection with PEEM experiments employing pulsed laser sources [22].

Here we present a systematic study on the influence of space charge effects in aberration corrected XPEEM instruments as observed with the SMART experiment, and consequently provide suggestions how to circumvent the negative effects that particularly occur in connection when using synchrotron light sources.

2. Instrumental set-up

The SMART instrument combining LEEM with PEEM is equipped with an aberration corrected magnetic Omega-type energy filter and with a tetrode electron mirror acting as an aberration corrector to compensate simultaneously for spherical and chromatic aberrations of the optical system, mainly of the objective lens [11].

2.1. Variety of electron sources

Three electron sources are routinely used: (a) a field emitter electron gun illuminates the specimen surface with a parallel electron beam; the elastically reflected electrons are imaged in the LEEM mode, such that surface structures, e.g. structural domains [23], local film thicknesses [24], and surface morphologies (single atomic steps [25], facets [26], etc.) are visualized by diffraction and interference contrast, (b) a short arc Hg-lamp is used in PEEM experiments to illuminate the sample with 4.9 eV photons (the image contrast is mainly caused by differences in the local work function [27,28]), and (c) soft x-rays from the BESSY synchrotron light source of the Helmholtz Center Berlin in the photon energy range from 100 eV to 1000 eV for XPEEM with spectroscopic contrast with (XPS, UPS) or without energy filtering (NEXAFS), which enables, e.g., local element mapping using the lateral resolution of the microscope [16,29].

Further possible sources have not been utilized with this instrument up to now, but might be implemented in the SMART in the future. By using an electron gun at a potential floating above the base potential of the microscope the inelastically reflected electrons can be used for example to enable – depending on the energy range of the imaged and the exciting electrons – SEEM (secondary electron emission microscopy), AEEM (Auger electron emission microscopy) [30] and local EELS (Electron energy loss spectroscopy). By using a (focused and – optionally – energy filtered) He-source local UPS is possible up to 40 eV [31]. A variety of Laser sources are already installed at other LEEM/PEEM systems to study 2ppe processes [32]. Further examples for possible emission sources are MEIS (metastable ion spectroscopy) and TEEM (thermal emission) [33].

Compared to other high resolution electron microscopes such as TEM and SEM, the PEEM/LEEM method excels by the high surface sensitivity of up to 0.5 nm depending on the kinetic electron energy at the specimen surface (typically between a few eV up to 500 eV). Because of the fast parallel (i.e. non scanning) detection, the UHV compatibility and the special design of the objective lens in front of the sample (allowing to dose gases and to deposit adsorbates from evaporators during operation), the LEEM/PEEM instruments are in general ideal tools to observe *in situ* and *in real time* a variety of surface processes, such as phase transitions [34], thin film growth [35,36], or surface reactions [27,37,38].

2.2. Multi-technique instrument

A major advantage of an energy filtered LEEM/PEEM instrument is the comprehensive characterization of objects on surfaces. Within a few seconds, the operator can switch between (energy filtered) microscopy, diffraction/band mapping from selected areas, which are only a micrometer small, and the angle-resolved spectroscopy from nanometer sized surface objects [13,16]. Additionally, the contrast mechanism can be altered within seconds, by changing the source, simply by opening the beam shutter of the photon source or by setting the deflector of the electron gun.

2.3. Electron path through the microscope

For the energy filtered XPEEM imaging, the monochromatic light of the beam-line illuminates a surface area of about 10 μm by 4 μm under grazing incidence. The full energy spectrum of electrons is emitted with a kinetic energy E_0 from 0 eV up to the photon energy $h\nu$ reduced by the work function, ϕ. These electrons are accelerated by the objective lens to a final kinetic energy of $eU_0 = 15{,}000$ eV. The following special magnetic beam splitter has high symmetry, so that it is both, free of dispersion and free of relevant aberrations. This device deflects the electron beam by 90° into an imaging electrostatic mirror, where via reflection chromatic and spherical aberrations are also induced. By optimizing the system settings [6], these additional aberrations can compensate for the other aberrations of the system (mainly of the objective lens) up to the third order. The aberration-compensated intermediate image is magnified by transfer optics into a magnetic Omega-type energy filter [39], which selects ~0.5 eV wide energy window from the energy spectrum for imaging. By using electrons from specific core levels, a magnified electron image of the surface with pure element contrast can thus be obtained at video rates on a two-dimensional detector. The detector consists of a pair of channel plates and a phosphor screen combined with a video rate CCD camera.

Instead of using a light source to excite photo-emitted electrons at the sample, an electron gun may be utilized to illuminate the sample with electrons. The elastically reflected electrons

establish images in the same way as in the case of XPEEM, but containing structural contrast.

2.4. Sample preparation

For the investigation of electron optical properties of the aberration corrected and energy filtered XPEEM we have chosen two different systems as test samples: thin Au patches on a W(110) surface and a dewetted Fe_3O_4 film on a Pt(111) surface.

The W(110) surface was cleaned by cycles of oxygen and high temperature treatment, which led to a flat surface with a few 100 nm wide terraces with single atomic steps. During our experiments CO adsorption on the W(110) surface was unavoidable and led to well ordered overlayers on parts of the surface, as identified by typical LEED patterns. On this surface about one monolayer of Au was deposited at 900 K in UHV, forming a one to two monolayer thick film with holes uncovered by Au. These test objects provided strong chemical contrast. Fig. 1 shows a special experiment as example comparing the LEEM and XPEEM modes with and without aberration-correction for different contrast apertures. In order to avoid thermal drift of the freshly prepared surface upon cooling, the sample was kept at elevated temperature of 750 K. At this temperature, Au layers rearrange so that holes in the film close which can be observed in the sequence of Fig. 1.

As mentioned above, the second test system is a 3 nm thin magnetite (Fe_3O_4) film on a Pt(111) surface. The substrate was cleaned by the standard procedure of repeated oxygen treatment, sputtering and annealing cycles. A completely closed oxide film was formed by two cycles of Fe deposition at room temperature and oxidation at 900 K with oxygen partial pressure of 1×10^{-6} mbar. By subsequent annealing up to 1000 K the film de-wetted and formed holes in which the Pt(111) surface was covered by only one layer of FeO (wüstite). A detailed description of this film preparation can be found in [40]. Also this test system offered strong chemical contrast at the Pt 4f XPS peak.

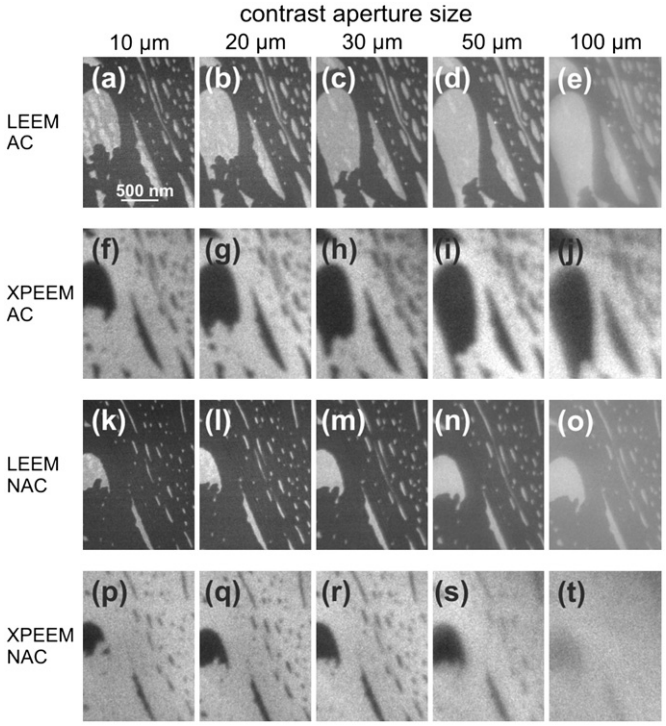

Fig. 1. LEEM (a–e, k–o) and XPEEM (f–j, p–t) images of an incomplete Au layer on W(110) at a kinetic electron energy of $E_0=113$ eV. XPEEM uses the Au 4f photoemitted electrons excited by photons with $h\nu=200$ eV. The top two rows show aberration corrected (AC), the bottom two non-corrected images (NAC). From the left to the right column the contrast aperture is increased from 10 µm to 100 µm. The image intensity scaling for LEEM and XPEEM images, respectively, is kept constant. To compensate for the change in image intensity, the acquisition time of the XPEEM images was matched to the area of the contrast aperture: 1800 s, 450 s, 200 s, 72 s and 18 s for f–j and p–t. The photon flux j_{ph} varied between 8×10^{11} ph/s and 5×10^{11} ph/s. The acquisition time in LEEM was always 50 s. The displayed field of view (*FoV*) was 1.5 µm × 2.0 µm the images were cut from the original FoV of 3.11 µm. The analyzed lateral resolution is plotted in Fig. 2.

2.5. Soft x-ray beamline

The SMART microscope is operated at the high-brilliance undulator beamline UE49-PGM-SMART at BESSY-II. The x-ray beamline optics focuses the light source onto the energy exit slit. A refocusing mirror de-magnifies the exit slit by a factor of 0.05 and illuminates the sample surface under grazing incidence, ideally producing a spot size 10 µm times 4 µm wide. A variable, so-called ID aperture behind the undulator insertion device reduces the acceptance angle of the emitted light at the beamline entrance. Therefore, the total photon intensity can be reduced from the maximum of 10^{13} ph/s to zero. At the same time the size of the illuminated area is only weakly affected. Because smaller angles limit the aberrations in the light optics, the image of the exit slit appears sharper in Fig. 3b (small ID aperture) compared to Fig. 3a (large ID aperture).

The experiments were carried out during two different operation modes of the BESSY ring. In the so-called "multi-bunch mode" 320 of the 400 possible "buckets" per ring cycle are filled and contribute to the light emission each producing a short light flash. The time duration of these flashes ranges from 40 to 100 ps, with off-times between two bunches of 2 ns. The ring current in our experiment was 200 mA; it is proportional to the overall photon flux. In the second operation mode, the so-called "single bunch mode", only one of the 400 "buckets" is filled, with a bunch length of 40 ps and a time between the circulating single bunches of 800 ns. [41] In this mode the ring current was 8 mA. The photon flux was measured using a calibrated GaAs diode directly behind the energy slit.

3. Experimental

3.1. Influence of aberrations on the lateral resolution and on the transmission

The effect of the aberration corrector has been analyzed by imaging an incomplete layer of gold on a W(110) surface (sample 1). Fig. 1 shows LEEM (a–e, k–o) and XPEEM images (f–j, p–t) of the same surface area but with different contrast aperture sizes in the range between 10 and 100 µm, corresponding to a variation of the acceptance angle between 28 mrad and 280 mrad. Because in XPEEM the area of the aperture is proportional to the transmission, the acquisition time Δt matches to the aperture size d_A by $\Delta t\sim1/{d_A}^2$ to keep the overall image intensity constant. As a consequence, the image acquisition time in XPEEM ranged from 18 s ($d_A=100$ µm) to 1800 s ($d_A=10$ µm). To avoid the influence of sample drift during this long acquisition time, 40 images of 45 s each were accumulated. Afterwards, the drift between the images was numerically compensated, and all images were added yielding the images shown. The quality of this matching process depended on the accuracy of identifying good reference points for drift compensation; it affected directly the lateral resolution. The overall measurement time for the sequence in Fig. 1 was 4:40 h (starting with (e) and finishing with (p)). In order to reduce the thermal drift after film preparation, the sample was kept at elevated temperature as mentioned above. During this time the

surface morphology changed due to a rearrangement of the Au film – the holes in the Au film (dark in XPEEM, bright in LEEM) shrank considerably. Nevertheless, this did not influence the estimation of lateral resolution.

The images shown in Fig. 1 were taken with two different settings of the electron mirror. Whereas for the upper two rows the voltages of the mirror were optimized to compensate for the spherical and the chromatic aberrations of the objective lens at $E_0=113$ eV (in the following this setting is called *aberration corrected mode* (AC)), the mirror setting for the lower two rows did not compensate for the overall aberrations. Therefore, we call the latter *non-aberration corrected mode* (NAC).

In both modes the sharpness of the image got worse for large aperture sizes. At large apertures the effect of aberration correction is clearly visible in XPEEM images (compare j with t). However, the LEEM images for the corrected and non-corrected mode do not differ at this magnification. The lateral resolution in each image was estimated at different cross-sections along the edge of the Au layer. The results are summarized in Fig. 2 for the corrected (blue data points) and non-corrected (black) modes; the resolution for XPEEM is shown as full symbols, for LEEM as open symbols. The theoretically expected resolution limits, d, for both modes are added as continuous lines. For the dashed curve a constant offset has been assumed.

In a simplified description, d is determined by a Gaussian convolution of different contributions [42]:

$$d=\left(\left(\frac{0.61\lambda}{\alpha}\right)^2+\left(\frac{1}{2}C_s\alpha^3\right)^2+(C_c\kappa\alpha)^2+(C_{cc}\kappa^2\alpha)^2 + (C_{cs}\kappa\alpha^3)^2+(C_{ss}\alpha^5)^2\right)^{1/2}$$

where the first part represents the diffraction limit increasing with decreasing acceptance angle α and limited by the aperture in the back focal plane. Here $\lambda\cong\sqrt{1.5/E_0}$ denotes the electron wave-length in nm with E_0 the kinetic electron energy in eV at the sample with respect to the vacuum level. C_s and C_{ss} are the third and fifth order spherical aberration coefficients and C_c, C_{cc} and C_{cs} are the coefficients for the different ranks of the chromatic aberration with a relative energy spread $\kappa=\delta E/E_0$ (δE is the energy spread of the electron beam, set in this case to $\delta E=0.5$ eV). In the corrected mode C_s and C_c are zero.

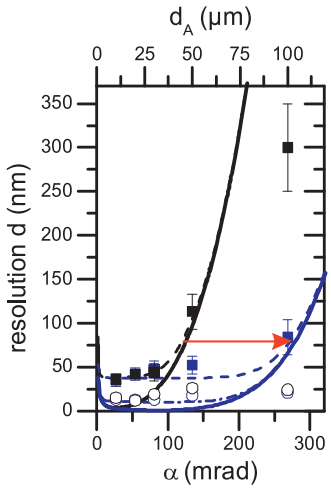

Fig. 2. Lateral resolution for the LEEM (open symbols) and XPEEM (solid symbols) images of Fig. 1 for AC (blue) and NAC (black), plotted versus the aperture size d_A, from which the acceptance angle α is calculated. The experimental data points are well described by the theoretically expected resolution limits (solid lines), especially if two different constant offsets are assumed (dashed and dash-dotted lines). (For interpretation of the references to color in this figure legend, the reader is referred to the web version of this article.)

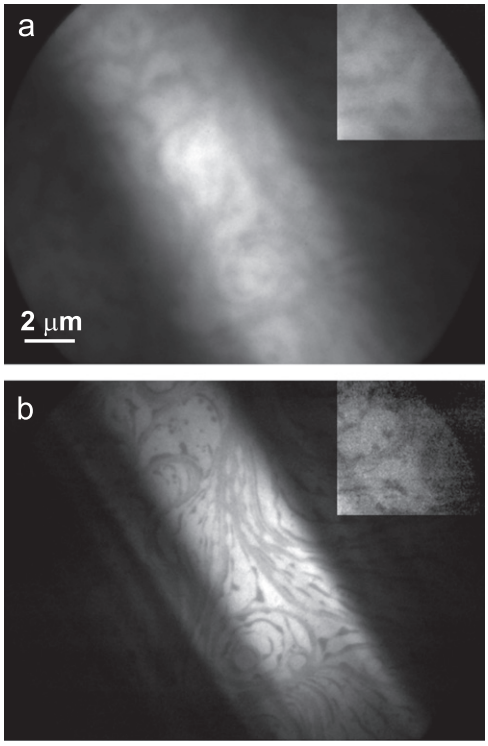

Fig. 3. XPEEM images of the illuminated sample area ($h\nu=167$ eV), taken with secondaries at $E_0=2$ eV with $\Delta E=0.5$ eV, set by the energy filter. The photon flux was 9×0^{12} ph/s and 0.8×10^{12} ph/s in (a) and (b), respectively. The image intensity scaling was 0–4000 cts (inset: 0–600) for (a) and 0–600 cts (inset: 30–80) for (b).

The graphs indicate two characteristic effects of the aberration corrector on the XPEEM images: (i) the increase in transmission by a factor of 5 at moderate resolution (see red arrow). In the corrected mode the same resolution of 80 nm can be reached by a more than twice as large contrast aperture compared to the uncorrected mode. (ii) An improvement of resolution is noticed at a large aperture of 100 μm, in which case 80 nm may be achieved with correction, but only about 300 nm without correction.

Whereas the theoretical prediction describes the behavior above 80 nm resolution in XPEEM images quite well, the resolution limits differ strongly at lower acceptance angle. The experimental data may be better described if a constant offsets d_0 is assumed (dashed curve).

$$d'=\left(d_0{}^2+d^2\right)^{1/2}$$

In contrast to the XPEEM results the LEEM resolution data do not depend significantly on the acceptance angle, as predicted by a geometric electron optical description [13]. The values range between 12 nm and 26 nm, although the instrument has already demonstrated a resolution of 2.6 nm in LEEM [6]. The main reasons for the worse LEEM resolution shown in Fig. 2 are the limitations imposed by the used detection system of channel-plates, phosphor screen, and CCD-camera, besides a slight defocus, possible vibrations, and sample drifts. Typically the number of resolved pixels in an image is about $N_p=300$, therefore on a 40 mm sized screen a detector resolution of 13 μm can be reached. As a consequence, at the overall field of view $FoV=3.11$ μm used in the LEEM images of Fig. 1 a detector limited resolution of $d_{\mathrm{det}}=FoV/N_p=10$ nm is expected, which is in good

agreement with our data, see dash-dotted line with assumed $d_0=10$ nm. At the largest aperture used in LEEM, however, the resolution is clearly better than expected according to the above estimate. The reason could be the difference between the geometrical description of the optics and the diffraction contrast at the investigated Au step. Due to the wave nature of the electrons, the resolution does not increase with the acceptance angle but is constant, as shown recently [43].

The major question, why the resolution achieved in XPEEM is so much worse than in LEEM, although identical electron optical setting were used, needs further investigation. The observed offset of about 40 nm in XPEEM resolution is far away from the detection limit of 10 nm in LEEM. A possible explanation could be the sample drift, which should have a strong influence at longer acquisition time, i.e. at small aperture sizes. However, we observed, that sample drift did not occur in this case. Furthermore, at 50 μm contrast aperture the acquisition time of XPEEM and LEEM is nearly identical, implying that the influence of sample drift should be the same in both cases. As we will show in the following section, space charge effects provide the proper explanation for our experimental findings.

3.2. Space charge effects

In order to study the influence of space charge effects, the photon flux of the beamline was varied over more than one order of magnitude. Fig. 3 shows two energy filtered XPEEM images taken at the intensity maximum of the secondary electrons at $E_0=2$ eV with an energy filter resolution set to 0.5 eV. Both images show the same area on the surface, but with different intensity of the illuminating x-ray beam. To improve the display, the detected image intensities were scaled up to their maximum. At the chosen low magnification, the elongated x-ray beam profile on the specimen surface can be observed. The long horizontal axis is rotated due to the magnetic objective lens. Clearly, the image at low illuminating beam intensity (Fig. 3b) is much sharper than that at high beam intensity (Fig. 3a). This observed strong effect of the photon beam intensity on the image resolution, may be explained by space charge effects [17], i.e. the Coulomb interaction between electrons in the electron beam which leads to a blurring of the image. In Fig. 3 we also compare the resolution in the center of the illuminated area within the image, with that in an area with less intensity, about 10 μm away from the maximum intensity. For this, the image intensity in the side wings of the intensity profile has been rescaled, shown in the insets in the upper right corners of each image such that the intensity scale for inset and layer image are equal. Remarkably, the resolution is the same for both, the intense center and the darker side areas. From these two observations we conclude that dominating space charge effects do not occur directly at the sample surface, because the lateral resolution would then be determined by the local photon flux on the sample surface. Hence the resolution in the beam center should be worse than in the less intense areas.

A significant difference between a LEEM and a XPEEM measurement is the time structure of the electrons injected into the imaging system. Whereas LEEM deals with an electron beam intensity continuous in time, the electron beam used to create XPEEM images is pulsed. This time structure is due the time structure of the synchrotron radiation source, producing x-ray light pulses at a length of 40 ps. In the so-called multi-bunch hybrid mode, 320 of 400 possible bunches per circle are filled and emit light with a delay between the pulses of 2 ns, which leads to basically the same time structure of the beam of photo-emitted electrons in the microscope. This means that the total electron intensity in XPEEM is compressed to 2% of the total time; the rest of the time there are no electrons available for imaging. As a consequence, the maximum electron intensity is 50 times higher than the average XPEEM intensity. This peak intensity leads to a blurring of the image, even though the average image intensity appears moderate and comparable with the continuous LEEM intensity, where space charge effects were not observed under the present experimental conditions. A further argument for the pulsed time structure as a reason for the enhanced space charge effect is the very good resolution of 5.4 nm achieved with an aberration corrected PEEM [5] which uses a highly intense but non-pulsed Laser light source.

In order to study the influence of the time structure of the illuminating photon beam in more detail, we compare the intensity dependence of the lateral resolution during the multi-bunch mode with that observed in the single bunch mode (full black and red data points in Fig. 4, respectively). In both cases, the resolution increases with intensity. Compared to the multi-bunch the image blurring in the single bunch mode occurs already at low photon flux. The reason is, that here the intensity is concentrated in one pulse, whereas in multi-bunch the flux is distributed over 320 pulses per circle. Therefore, we normalized the data in the multi-bunch to the flux per bunch (see MB*, open black data points in Fig. 4). Now the two sets of data fit well together. From this observation it is clear that the overall beam intensity does not determine the space charge effect, but it is the photon flux, i.e., the intensity per time, which is of crucial importance.

3.3. Reducing space charge effects by a field aperture

Clearly, all electrons present in the beam per unit time contribute to space charge effects; however, not all electrons in the beam contribute to the image. Thus, those not contributing should be cut out. Therefore, we inserted a field aperture at the position of the first intermediate image in front of the beam splitter, which selected a surface area of 5 μm in diameter, whereas the area illuminated by the x-rays was about 30 μm to 10 μm in this experiment. This led to a reduction of the overall electron beam intensity of more than a factor 10. However, the intensity in the image at the field of view of 4 μm was not reduced by this field aperture. The presence of the aperture led to a strong improvement of the lateral resolution, as shown in Fig. 5a and b, for which we used a Fe_3O_4 film (sample 2) with holes as test system. The overall electron intensity was proportional to the

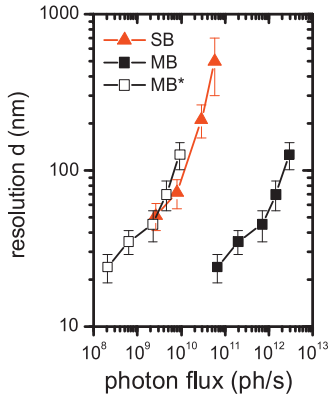

Fig. 4. Effect of the pulsed time structure: dependence of the XPEEM resolution on photon flux for multi-bunch (MB) and single bunch (SB) operation. For MB* the photon flux is normalized to one bunch. The XPEEM resolution was derived from images taken with Au $4f_{5/2}$ electrons at $E_0=113$ eV at $FoV=6.11$ μm in MB mode and with W $4f_{3/2}$ electrons at $E_0=165.5$ eV at FoV=12.4 μm. In both cases, the contrast aperture was $d_A=30$ μm and the energy resolution $\Delta E=0.5$ eV. AC was optimized for the used energy range. (For interpretation of the references to color in this figure legend, the reader is referred to the web version of this article.)

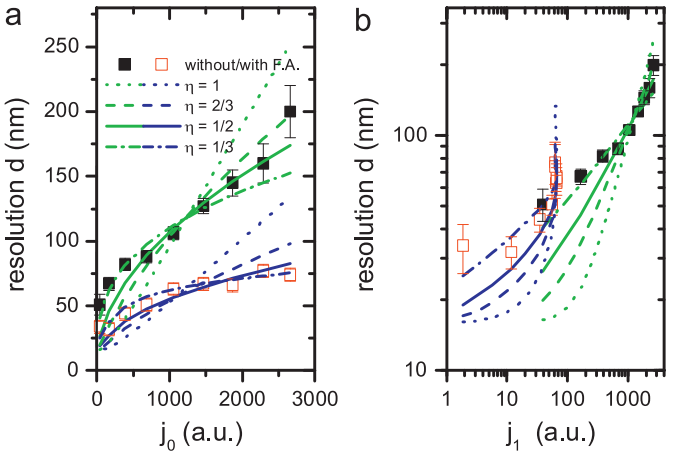

Fig. 5. Influence of the electron beam current on the lateral resolution, (a) and (b) in front of and behind the field aperture (F.A.), respectively. For the full black data points the entire beam intensity j_0 passes the system up to the contrast aperture, whereas for the open red data the F.A. was introduced into the first intermediate image plane, reducing the overall beam current to j_1. Kinetic energy of the electrons was E_0=2.8 eV, photon energy $h\nu$=180 eV, energy slit was set to 0.5 eV, and the contrast aperture had a diameter of 30 μm. The photon flux was varied between $j_{ph}=1\times10^{11}$ ph/s and 7×10^{12} ph/s. The various lines depend on the choice of the exponent η and are described by the formula for d given in the text. (For interpretation of the references to color in this figure legend, the reader is referred to the web version of this article.)

photon flux of the illuminating x-ray beam, which was varied over a wide range.

In Fig. 5 the resolution d is plotted versus the initial electron beam current j_0 at the sample surface (Fig. 5a, linear scales) and the identical data d versus the electron beam current j_1 behind the field aperture (Fig. 5b, logarithmic scales). Clearly, for the same photon flux, and, therefore, the same initial electron flux j_0, the field aperture improves the lateral resolution by a factor of about 2. This demonstrates that a strong contribution to space charge effects occurs on the electron path behind the field aperture, very likely at the cross-overs in the beamsplitter and at the reverse point in the electron mirror. Nevertheless, the number of electrons between the sample surface and the field aperture still plays a role. This is documented by the increase of resolution with field aperture above j_0=1500 cts in Fig. 5a, or correspondingly at j_1=80 cts in Fig. 5b (red open data points). Here the opening of the ID aperture causes only a broadening of the illuminated spot, but no intensity increase in the center of the spot. This means, the initial intensity j_0 is increased, but not the intensity j_1 passing the field aperture. In this context we like to mention that between the lowest and the highest intensity the excitation of the objective lens had to be continuously increased by about 0.7‰ to optimize the focus. This may be explained by the space charge defocus as described in Ref. [21].

The resolution data d can be described by a Gaussian convolution of two power laws and the detection limit d_0:

$$d=\left((Aj_0{}^{\eta})^2+(Bj_1{}^{\eta})^2+d_0{}^2\right)^{1/2}$$

where $j_1=j_0$ for the case, when no field aperture is used. The best fitting exponent to describe both curves in Fig. 5a and b is $\eta=1/2$, which is in agreement with the theoretical prediction of Refs. [44,45]. In contrast, the experimental data in [17] can be described by a linear dependence. For $\eta=1/2$, the ratio B/A is about 2, indicating a stronger influence of the space charge on the path behind the field aperture compared to the path between sample and field aperture.

In the experiments described above, a sample current corresponding to the total amount of photo-emitted electrons was measured. We found that at the data point j_0=2000 cts the photocurrent corresponds to about 600 electrons in one pulse. From this value one can derive, that at the lowest j_1 value used only one electron per pulse passed the field aperture. This is the "one electron case", where no space charge can occur – assuming that consecutive pulses are well separated and cannot interact with each other. However, the image is still affected by space charge, because about 10 interacting electrons are in the electron cloud between surface and field aperture.

3.4. Resolution limit in energy filtered XPEEM

Based on the knowledge of aberration correction and space charge effects we optimized the set-up to gain a better lateral resolution e.g., by reducing the photon flux, increasing the acquisition time, and increasing the magnification to reduce the limitation by the detector. Also, a field aperture was inserted at the position of the first intermediate image. To avoid the influence of the thermal drift, again sets of images were taken at short acquisition time and were afterwards summed up including a numerical shift compensation of the image drift, as already described in Section 3.1. This procedure results in 100 images of 30 s time duration each, leading to a total acquisition time of 3000 s and an image as shown in Fig. 6b. The image was taken with the W4f XPS-peak at E_0=165.2 eV (sample 1), which represents pure elemental contrast. The cross-section through the border between a Au domain and the W substrate along the

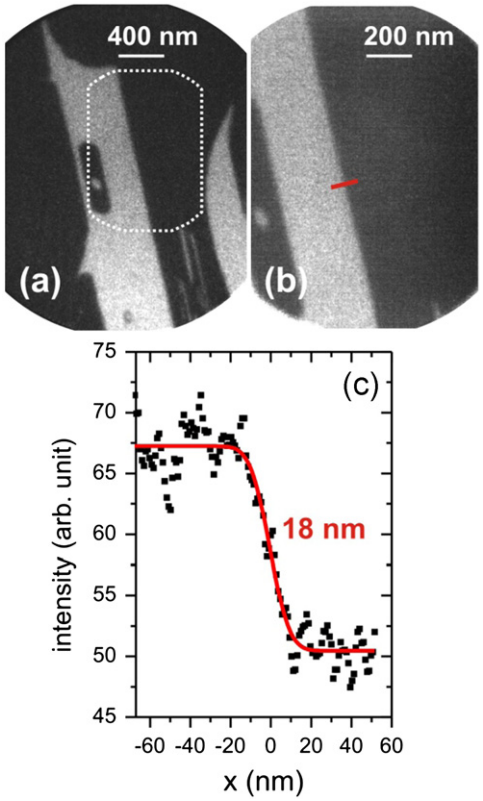

Fig. 6. Lateral resolution in XPEEM using W 4f at kinetic electron energy of E_0=165.2 eV, photon energy of $h\nu$=200 eV, photon flux $j_{ph}=8\times10^{11}$ ph/s (a) and 2×10^{11} ph/s (b), contrast aperture d_A=30 μm, and an acquisition time of 200 s (a) and 3000 s (b). The Au covered areas appear dark in the XPEEM images, whereas the W substrate is bright. (b) is a zoom-in of the overview image (a) (see marked area). The graph in (c) shows a cross section at the border between substrate and Au domain (red line in b). The fit with an Error-function yields in a lateral resolution of 18 nm. (For interpretation of the references to color in this figure legend, the reader is referred to the web version of this article.)

red line is displayed in Fig. 6c. The fit by an Error-function results in a lateral resolution of 18 nm.

The advantage of this specimen is the strong chemical contrast of a flat object, which is not affected by the morphology of the surface [46]. Quite often [16,47,48], three-dimensional islands are taken as a test object to measure the resolution. Compared to an atomically thin Au layer, these thick three-dimensional objects have an even larger chemical contrast to the surrounding area, but due to the height of a few tens of nanometer, the electric field in front of the sample is distorted giving rise to an abnormal local distortion of the image. Furthermore, the x-ray illumination under grazing incidence may be affected by this topography, on the side of the incoming light [49] as well as on the opposite side due to the light shadow [50].

The demonstrated resolution of 18 nm in Fig. 6 is the best value reported for an XPEEM with chemical contrast up to now. Locatelli et al. [47] reports a resolution of 50 nm for the same system (incomplete Au layer on W(110)), but with lower magnification and using the Au 4f intensity. In the same paper the resolution of 35 nm was shown using secondary electrons and Pb 5d photoelectrons. As a test system about 30 nm high three dimensional Pb islands were used. A similar system with three dimensional Ag islands was used to demonstrate a lateral resolution of 22 nm with secondary electrons [16].

4. Discussion of space charge effect

As already pointed out in Section 3.1, the explanation why the XPEEM resolution is always worse than the LEEM resolution, although the identical electron optical settings (lenses, apertures, energy width) are being used, is the space charge effect occurring for a very intensive electron beam. At first, this appears to be contradictory to the fact that the image intensity of LEEM is about four times higher than that in XPEEM. There are, however, three main differences between the LEEM and the XPEEM mode: (i) the energy distribution, (ii) the time structure, and (iii) the angular distribution of the reflected (LEEM) and the emitted (XPEEM) electrons.

In LEEM the beam contains elastically reflected electrons with a narrow energy width (typical energy width between 0.3 and 0.7 eV, depending on the kind of electron source) and secondary electrons with a wide distribution around a kinetic energy of approx. 3 eV. Whereas only the former contribute to the image, the latter are cut off by the contrast aperture and/or by an energy filter. For a clean and defect free surface the effect of secondary processes is relatively small in LEEM: typically only half of the electrons are secondaries. On the contrary, in XPEEM the intensity of the secondary electrons in the energy ranges between 0 and approx. 50 eV is high, i.e. between 70% and 90% of the overall intensity. If an XPS core level peak is used, the intensity of the peak which has a width of about 0.3–1 eV is only a few percent of the total number of emitted electrons. This means that only a minor part of the XPEEM electron beam is used for imaging, the rest is cut off by the energy filter. Nonetheless, the charge of the majority of the electrons disturbs the imaging and leads to blurring.

Whereas the reflected beams in LEEM show a very narrow angular spread (less than 1°), the photo-emitted electrons have a more or less continuous distribution over the whole solid angle. Because the aberrations of the electron optics reduce the acceptance angle to a few degrees, only the inner part (typically only 0.1–1% of the total intensity) of the emission cone can be used for imaging – the major part of the emitted electrons is cut off by the contrast aperture limiting the acceptance angle. On the contrary, in LEEM this aperture selects one of the few sharp LEED spots, therefore typically more than 10% of the elastically reflected intensity is used for imaging. Again the argument counts, that in XPEEM most of the electrons are not being used, but disturb the imaging electrons by their charge. Here the aberration correction already improves the situation by enlarging the transmission by about one order of magnitude. Therefore, instead of 0.01% in a non-corrected system, about 0.1% of the emitted electrons can be used in corrected systems (in a typical kinetic energy range between 30 and 100 eV).

The most critical difference is the different time structure, as already discussed by Locatelli et al. [17]. Whereas LEEM makes use of a continuous flux of electrons, the XPEEM intensity is pulsed due the time structure of the exciting x-ray beam with a pulse length at BESSY of typically 40 ps and a pulse distance of 2 ns. As a consequence, the maximum pulse intensity in XPEEM is higher than the constant LEEM intensity, though the average intensity is lower. As an example, if the average XPEEM image is four times weaker compared to the LEEM image, the peak intensity is still 13 times higher than the average LEEM intensity. This high peak intensity and the related high space charge density cause most of the image blurring in XPEEM.

In the following we discuss, in particular, the influence of the different cross-overs of the electron beam on the path between the sample surface and the intensity limiting contrast aperture, assuming that those areas determine the space charge effect. Due to the high charge density, it is likely that those cross-overs are the most critical for the space charge effect. A schematic drawing of the electron path is given in Fig. 7, where the beam diameter is scaled by a factor of 40 in order to visualize the focusing effect. The blue beam represents the α bundle, with trajectories starting at the sample surface on axis, however with varying angles, whereas the trajectories of the γ bundle (green) start parallel with respect to the axis, however at varying surface positions. The first cross-over is located in the back focal plane of the objective lens, the diameter of which is, in the case of the SMART microscope, $d_{BFP} = 200\,\mu m\sqrt{E_0(eV)}$ for the initial kinetic energy E_0 at the sample surface. The second cross over is in the first intermediate image plane at the entrance of the magnetic beam splitter, with a diameter of $d_{IIP}=Md_0$ at a magnification of $M=18$ and the size of the emitting area d_{em}. The example in

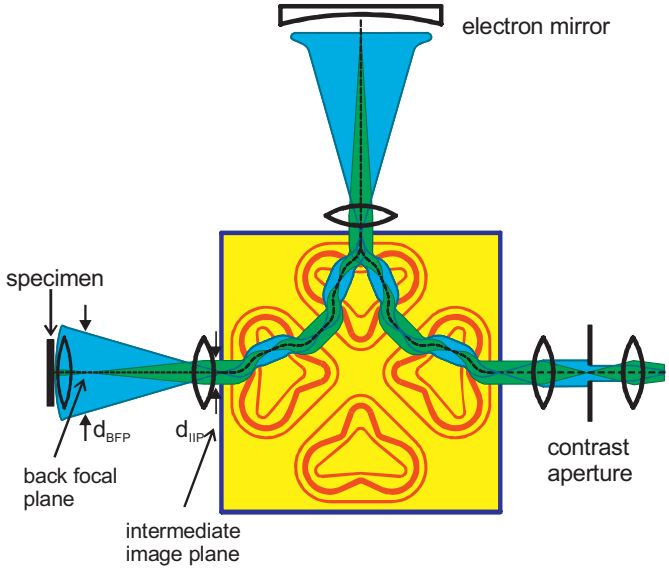

Fig. 7. Scheme of the electron beam paths through the electron optics between specimen and contrast aperture. The blue and green beams are the α and γ bundles, respectively. (For interpretation of the references to color in this figure legend, the reader is referred to the web version of this article.)

Fig. 7 shows a typical situation for XPEEM, with $E_0=100$ eV and a final energy of 15,000 eV and for $d_{em}=30$ μm. In case of a lower initial kinetic energy, the cross over in the back focal plane is smaller (e.g., 200 μm for $E_0=1$ eV compared to 2000 μm for $E_0=100$ eV); however, the diameter of the intermediate image plane is independent of the initial energy. In spite of three cross overs the beam diameter in the beam-splitter is nearly constant at about 500 μm. Clearly, there is no cross-over smaller than the initial beam size of 30 μm at the sample surface. Especially the size of the back focal plane and the beam size at the mirror – on which the back focal plane is imaged – are large compared to the rest of the beam. As a consequence one can state, that along the path between objective lens and contrast aperture there is no special cross-over with significantly large space charge densities which may cause local image blurring. Instead, the blurring occurs along the entire path. Nevertheless, critical areas might be the specimen surface and the electron mirror, because here the kinetic energy is very low compared to the rest of the microscope with $eU_0=15{,}000$ eV. Whereas the kinetic energy at the sample surface is distributed over an entire spectrum – a typical range of E_0 is 0 to 200 eV – all electrons are decelerated down to 0 eV in the mirror. This implies that these electrons are very sensitive to space charge effects. However, the beam diameter here is one to two orders of magnitude larger than at the sample surface leading to a lower charge density. The question therefore arises: is the long path at higher kinetic energy of 15,000 eV or are the short parts of trajectories at low kinetic energy at the sample and at the mirror decisive for space charge effects? The determining factor for the space charge effect is the time, the electrons need to pass through a given area of high electron density, because this sets the time for interaction between the charged particles. Initially, at the sample surface all emitted electrons start in one 40 ps short pulse and are accelerated in the field of the objective lens from the sample potential U_0 toward 0 V. After passing the constant potential, these electrons are decelerated at the mirror and accelerated after reflection. The faster electrons will reach the mirror earlier than the slower electrons. The time t for passing the three different sections and the delay time Δt between the electron pulses with the initial energy of $E=E_0$ and $E=0\,eV$ can be estimated. With $v_B=\sqrt{2eU_0/m}$ (e and m are electron charge and mass) and simplifying the electric field in front of the sample and the electron mirrors by assuming uniform acceleration fields, one can derive for the acceleration in front of the sample with field length l:

$$t_{acc}=2\frac{l}{v_B}\left\{\sqrt{1+\frac{E_0}{eU_0}}-\sqrt{\frac{E_0}{eU_0}}\right\}\approx 2\frac{l}{v_B}\left\{1-\sqrt{\frac{E_0}{eU_0}}\right\}$$

$$\Delta t_{acc}=2\frac{l}{v_B}\left\{1-\sqrt{1+\frac{E_0}{eU_0}}+\sqrt{\frac{E_0}{eU_0}}\right\}\approx 2\frac{l}{v_B}\sqrt{\frac{E_0}{eU_0}}$$

For the section of length D with constant potential between objective lens and electron mirror:

$$t_{const}=\frac{D}{v_B}\frac{1}{\sqrt{1+(E_0/eU_0)}}\approx\frac{D}{v_B}\left(1-\frac{1}{2}\frac{E_0}{eU_0}\right)$$

$$\Delta t_{const}=\frac{D}{v_B}\left\{1-\frac{1}{\sqrt{1+(E_0/eU_0)}}\right\}\approx\frac{1}{2}\frac{D}{v_B}\frac{E_0}{eU_0}$$

and finally for the deceleration to the reverse point of the electron mirror (field length L):

$$t_{dec}=2\frac{L}{v_B}\sqrt{1+\frac{E_0}{eU_0}}\approx 2\frac{L}{v_B}\left(1+\frac{1}{2}\frac{E_0}{eU_0}\right)$$

$$\Delta t_{dec}=2\frac{L}{v_B}\left\{1-\sqrt{1+\frac{E_0}{eU_0}}\right\}\approx-\frac{L}{v_B}\frac{E_0}{eU_0}$$

The time length of 40 ps for the electron pulse corresponds to a lateral length of 2.9 mm along the axis in the constant 15,000 eV regime and the period of 2 ns causes a distance between two neighbored electron clouds of 145 mm.

Table 1
Time of flight and delay time for an electron pulse with $E_0=100$ eV initial kinetic energy between sample surface and electron mirror. The delay time is the time difference of the electron pulses with initial energy 0 eV and 100 eV.

Section	Length of section (mm)	Time of flight t (ps)	Delay time Δt (ps)
Acceleration in objective lens	3	77	6
Constant potential (0 V)	700	9600	32
Deceleration in mirror	6	165	−0.56
Overall time		9840	37

The passing time and the delay time of each section are listed in Table 1. Clearly, most of the travel time (about 10 ns) the electrons are at a kinetic energy of 15,000 eV; only for 77 ps and for 165 ps the beam spends in regions of acceleration in front of the specimen and deceleration in the electron mirror. From this one may conclude, that the blurring due to space charge is caused along the long path, and not along the short paths at small kinetic energy. An interesting point is the delay time: consider that after about 70 cm an electron pulse at 100 eV is separated from its secondary electrons (around 3 eV) by the pulse length. This implies that the 100 eV electrons used for energy filtered imaging do not overlap with the very intense secondary electrons. Laterally they are more than 2.9 mm apart from each other. Therefore, it must be concluded, that the space charge effect, mainly caused by the very intense secondary electrons, takes place only along the initial 70 cm along the microscope axis. Behind this point the interaction between the secondaries and the core level electrons can be neglected. As a consequence, the electrons at 100 eV kinetic energy and the secondary electrons are not reflected at the same time in the mirror. Therefore, the electron mirror itself does not have an additional negative space charge effect.

5. Conclusion and outlook

The corrector compensates for spherical and chromatic aberrations, as already shown in LEEM with a resolution of 2.6 nm [6]. In XPEEM the strongest effect can be seen at larger acceptance angles (set by the contrast aperture) with an improvement of the resolution by a factor of 4, whereas the transmission increases by more than a factor of 5 at a moderate resolution of 80 nm, which fits well to the theoretical expectation at this lateral resolution. Theoretically, the optimum lateral resolution due to aberrations (at 100 eV with an energy width of $\Delta E=0.5$ eV) is 3.8 nm (transmission $T=0.23\%$) with NAC and 0.96 nm ($T=2.3\%$) with AC. This means an improvement in resolution by a factor of 4 and a transmission enhancement by factor 10. At a resolution of 3.8 nm with AC the transmission equals 6.9%, i.e. a gain of factor 30.

However, the experimental, lateral resolution in XPEEM is limited to about 18 nm by space charge effects, which can only be surpassed by reduction of the emitted electron flux. This should be done as early as possible, because the space charge induced blurring occurs along the entire path up the contrast aperture. In our case, we used both a small field aperture in the intermediate image plane to reduce the electron density in the imaging column, and the exciting x-ray beam by apertures in the beamline. As a result, we limited the electron density behind the field aperture down to only one electron per pulse, which is the ideal case, where no interaction of charged particles can occur.

We suggest four options – some of these are already discussed in Ref. [17] – to improve the situation further. If each of these

options can reduce the maximum peak intensity of the electron beam by a factor of 2, then the overall effect would be a reduction factor of $2^4=16$. This means that the peak intensity would be comparable with the continuous beam intensity in LEEM, so that a lateral resolution below 5 nm can be expected.

The suggested options affect different regions of the spectromicroscope: (i) The pulsed *time structure* of the synchrotron light source is the main origin for the resolution limiting effect of the space charge. Longer pulses or more bunches per circle would relax the difficulties. (ii) The x-ray *illumination optics* should be improved by producing a smaller focus on the sample surface: ideally, just the area of the investigated field of view should be illuminated, in order to avoid the creation of "useless" electrons outside the field of view. (iii) The flux of the *electron beam* should be reduced at the entrance of the microscope as soon and as much as possible to avoid the space charge effect on the path to the electron mirror. This may be done by placing apertures in the back focal plane to cut away large emission angles not used for imaging. Further apertures should be placed in the intermediate image plane, to select only the inner part of the surface image, to avoid electrons outside the detected field of view, and in the dispersive plane inside the beam splitter, in order to select the imaged core level electron and to filter out the disturbing secondaries. (iv) Finally, an improved *detection system* with a higher sensitivity and a larger number of detection pixels should be used – so that the acquisition time and/or the photon intensity can be reduced. Projects have been started to develop the next generation of detectors [51,52] with an improved detective quantum efficiency (DQE) [53].

These measures to reduce the space charge effect, together with a higher stability (due to longer acquisition time in case of a reduced flux), will result in a higher resolution. Although the electron mirror, which we use as an aberration corrector, is sensitive to space charge effects, the advantages of aberration correction overweigh this disadvantage. Due to the increase in transmission, a larger portion of the photo-emitted electrons can be used for imaging. Therefore the photon-flux and hence the space charge effect can be reduced. Based on these suggested options, a new spectromicrope (SMART-2) is under construction, which – besides higher stability of the mechanics and electronics, easier maintenance and improved user friendly control – implements the above discussed possibilities to reduce the space charge effects.

Acknowledgment

The authors thank for fruitful discussions with Florian Maier. We gratefully acknowledge the financial support by the Federal German Ministry of Education and Science (BMBF) under Contract no. 05 KS4WWB/4 and the technical support by the BESSY-II crew. The microscope is installed at the BESSY-II storage ring of the Helmholtz-Center Berlin for Material and Energy. HJF thanks the German Science Foundation (DFG) through Sonderforschungsbereich 546 and the Cluster of excellence UniCat, as well as Fonds der Chemischen Industrie.

References

[1] M. Haider, S. Uhlemann, E. Schwan, H. Rose, B. Kabius, K. Urban, Electron microscopy image enhanced, Nature 392 (1998) 768–769.
[2] O.L. Krivanek, N. Dellby, A.R. Lupini, Towards sub-Å electron beams, Ultramicroscopy 78 (1999) 1–11.
[3] B. Freitag, S. Kujawa, P.M. Mul, J. Ringnalda, P.C. Tiemeijer, Breaking the spherical and chromatic aberration barrier in transmission electron microscopy, Ultramicroscopy 102 (2005) 209–214.
[4] J. Zach, M. Haider, Aberration correction in a low voltage SEM by a multipole corrector, Nuclear Instruments and Methods in Physics Research Section A: Accelerators, Spectrometers Detectors and Associated Equipment 363 (1995) 316–325.
[5] R. Könenkamp, R.C. Word, G.F. Rempfer, T. Dixon, L. Almaraz, T. Jones, 5.4 nm spatial resolution in biological photoemission electron microscopy, Ultramicroscopy 110 (2010) 899–902.
[6] T. Schmidt, H. Marchetto, P.L. Lévesque, U. Groh, F. Maier, D. Preikszas, P. Hartel, R. Spehr, G. Lilienkamp, W. Engel, R. Fink, E.D. Bauer, H. Rose, E. Umbach, H.J. Freund, Double aberration correction in a low energy electron microscope, Ultramicroscopy 110 (2010) 1358–1361.
[7] R.M. Tromp, J.B. Hannon, A.W. Ellis, W. Wan, A. Berghaus, O. Schaff, A new aberration-corrected, energy-filtered LEEM/PEEM instrument. I. Principles and design, Ultramicroscopy 110 (2010) 852–861.
[8] Two aberration corrected LEEM instruments are already commercially available: SPECS GmbH, 〈http://www.specs.de/〉, and ELMITEC GmbH, 〈http://www.elmitec.de/〉.
[9] E. Bauer, LEEM and UHV-PEEM: a retrospective, Ultramicroscopy, 119 (2012) 18–23.
[10] Both systems are installed at BESSY-II in Berlin, the second one is the commercialized version of Ref. [7] operated by the FZ Jülich group of C.M Schneider.
[11] R. Fink, M.R. Weiss, E. Umbach, D. Preikszas, H. Rose, R. Spehr, P. Härtel, W. Engel, R. Degenhardt, R. Wichtendahl, H. Kuhlenbeck, W. Erlebach, K. Ihmann, R. Schlögl, H.J. Freund, A.M. Bradshaw, G. Lilienkamp, T. Schmidt, E. Bauer, G. Benner, SMART: a planned ultrahigh-resolution spectromicroscope for Bessy II, Journal of Electron Spectroscopy and Related Phenomena 84 (1997) 231–250.
[12] R. Wichtendahl, R. Fink, H. Kuhlenbeck, D. Preikszas, H. Rose, R. Spehr, P. Hartel, W. Engel, R. Schlögl, H.-J. Freund, A.M. Bradshaw, G. Lilienkamp, T. Schmidt, E. Bauer, G. Benner, E. Umbach, SMART: An aberration-corrected XPEEM/LEEM with energy filter, Surface Review and Letters 5 (1998) 1249–1256.
[13] T. Schmidt, U. Groh, R. Fink, E. Umbach, O. Schaff, W. Engel, B. Richter, H. Kuhlenbeck, R. Schlögl, H.J. Freund, A.M. Bradshaw, D. Preikszas, P. Hartel, R. Spehr, H. Rose, G. Lilienkamp, E.D. Bauer, G. Benner, XPEEM with energy-filtering: advantages and first results from the SMART project, Surface Review and Letters 9 (2002) 223–232.
[14] R.M. Tromp, Measuring and correcting aberrations of a cathode objective lens, Ultramicroscopy 111 (2011) 273–281.
[15] G.F. Rempfer, A theoretical study of the hyperbolic electron mirror as a correcting element for spherical and chromatic aberration in electron optics, Journal of Applied Physics 67 (1990) 6027–6040.
[16] T. Schmidt, S. Heun, J. Slezak, J. Diaz, K.C. Prince, G. Lilienkamp, E.D. Bauer, SPELEEM: combining LEEM and spectroscopic imaging, Surface Review and Letters 5 (1998) 1287–1296.
[17] A. Locatelli, T.O. Menteș, M.Á. Niño, E. Bauer, Image blur and energy broadening effects in XPEEM, Ultramicroscopy 111 (2011) 1447–1454.
[18] T. Yasue, A. Nakeguchi, M. Hascimoto, T.O. Mentes, A. Locatelli, E. Bauer, T. Koshikawa, in: Proceedings of 6th International Symposium on Atomic Level Characterization for New Materials and Devices 2007, JSPS, 2007, pp. 207–211.
[19] P.W. Hawkes, E. Kasper, Space Charge Effects, Academic Press Ltd., London, 1989, pp. 954–970.
[20] H. Boersch, Experimentelle Bestimmung der Energieverteilung in thermisch ausgelösten Elektronenstrahlen, Zeitschrift für Physik A Hadrons and Nuclei 139 (1954) 115–146.
[21] P. Kruit, G.P. Jansen, Space charge and statistical coulomb effects, in: J. Orloff (Ed.), Handbook of Charged Particle Optics, CRC Press, 2008, pp. 341–391.
[22] N.M. Buckanie, J. Göhre, P. Zhou, D v.d. Linde, M.H.-v. Hoegen, F.J.M.z. Heringdorf, Space charge effects in photoemission electron microscopy using amplified femtosecond laser pulses, Journal of Physics: Condensed Matter 21 (2009) 314003.
[23] E. Bauer, Low energy electron microscopy, Reports on Progress in Physics 57 (1994) 895–938.
[24] W.F. Chung, Y.J. Feng, H.C. Poon, C.T. Chan, S.Y. Tong, M.S. Altman, Layer spacings in coherently strained epitaxial metal films, Physical Review Letters 90 (2003) 216105.
[25] W.F. Chung, M.S. Altman, Step contrast in low energy electron microscopy, Ultramicroscopy 74 (1998) 237–246.
[26] M. Horn-von Hoegen, F.J.Meyer zu Heringdorf, D. Kähler, T. Schmidt, E. Bauer, Adsorption induced giant faceting of vicinal Si(001), Thin Solid Films 336 (1998) 16–21.
[27] H.H. Rotermund, W. Engel, M. Kordesch, G. Ertl, Imaging of spatio-temporal pattern evolution during carbon monoxide oxidation on platinum, Nature 343 (1990) 355–357.
[28] E. Bauer, M. Mundschau, W. Swiech, W. Telieps, Surface studies by low-energy electron microscopy (LEEM) and conventional UV photoemission electron microscopy (PEEM), Ultramicroscopy 31 (1989) 49–57.
[29] A. Locatelli, E. Bauer, Recent advances in chemical and magnetic imaging of surfaces and interfaces by XPEEM, Journal of Physics: Condensed Matter 20 (2008) 093002.
[30] E. Bauer, C. Koziol, G. Lilienkamp, T. Schmidt, Spectromicroscopy in a low energy electron microscope, Journal of Electron Spectroscopy and Related Phenomena 84 (1997) 201–209.
[31] R.M. Tromp, Y. Fujikawa, J.B. Hannon, A.W. Ellis, A. Berghaus, O. Schaff, A simple energy filter for low energy electron microscopy/photoelectron emission microscopy instruments, Journal of Physics: Condensed Matter 21 (2009) 314007.

[32] F.J.Meyer zu Heringdorf, L.I. Chelaru, S. Möllenbeck, D. Thien, M. Horn-von Hoegen, Femtosecond photoemission microscopy, Surface Science 601 (2007) 4700–4705.
[33] M. Mundschau, Emission microscopy and surface science, Ultramicroscopy 36 (1991) 29–51.
[34] J.B. Hannon, R.M. Tromp, Low-energy electron microscopy of surface phase transitions, Annual Review of Materials Research 33 (2003) 263–288.
[35] F.-J.Meyer zu Heringdorf, M.C. Reuter, R.M. Tromp, Growth dynamics of pentacene thin films, Nature 412 (2001) 517–520.
[36] T. Schmidt, E. Bauer, Interfactant-mediated quasi-Frank-van der Merwe growth of Pb on Si(111), Physical Review B 62 (2000) 15815–15825.
[37] T. Schmidt, A. Schaak, S. Günther, B. Ressel, E. Bauer, R. Imbihl, In situ imaging of structural changes in a chemical wave with low-energy electron microscopy: the system Rh(110)/NO+H2, Chemical Physics Letters 318 (2000) 549–554.
[38] H.H. Rotermund, Real time imaging of catalytic reactions on surfaces: Past, present and future, Surface Science 603 (2009) 1662–1670.
[39] S. Lanio, H. Rose, D. Krahl, AND TEST, Improved Design Of A Corrected Imaging Magnetic Energy Filter, Optik 73 (1986) 56–68.
[40] A. Sala, H. Marchetto, Z.H. Qin, S.S. Shaikhutdinov, Th. H.-J. Freund, Defects and inhomogeneities in Fe_3O_4(111) thin film growth on Pt(111), Physical Review B 86 (2012) 155430.
[41] 〈http://www.helmholtz-berlin.de〉, search for "operating modi".
[42] P.W. Hawkes, E. Kasper, Basic Geometrical Optics, Academic Press, London, 1989.
[43] S.M. Schramm, A.B. Pang, M.S. Altman, R.M. Tromp, A contrast transfer function approach for image calculations in standard and aberration-corrected LEEM and PEEM, Ultramicroscopy 115 (2012) 88–108.
[44] G.A. Massey, M.D. Jones, B.P. Plummer, Space-charge aberrations in the photoelectron microscope, Journal of Applied Physics 52 (1981) 3780–3786.
[45] J.C. Lovegren, G.A. Massey, Monte Carlo simulation of discrete space charge effects in photoelectron emission microscopy, Microscopy and Microanalysis 3 (1997) 214–223.
[46] E. Bauer, in: Himeji, Discussion at the 6th Conference on LEEM/PEEM, 2006.
[47] A. Locatelli, L. Aballe, T.O. Mentes, M. Kiskinova, E. Bauer, Photoemission electron microscopy with chemical sensitivity: SPELEEM methods and applications, Surface and Interface Analysis 38 (2006) 1554–1557.
[48] A. Oelsner, A. Krasyuk, S. Nepijko, C.M. Schneider, G. Schönhense, Spatially resolved observation of dynamics in electrical and magnetic field distributions by means of a delayline detector and PEEM, Journal of Electron Spectroscopy and Related Phenomena 144–147 (2005) 771–776.
[49] P. Kirschbaum, N.M. Buckanie, F.-J.M.Z. Heringdorf, Impact of C-60 adsorption on surface plasmon polaritons on self-assembled Ag(111) islands on Si(111), Plasmonics 7 (2012) 229–233.
[50] T. Schmidt, J. Slezak, S. Heun, J. Diaz, R.R. Blyth, R. Delaunay, D. Cocco, K.C. Prince, E. Bauer, M. Coreno, Optical layout of a beamline for photoemission microscopy, Journal of Synchrotron Radiation 6 (1999) 957–963.
[51] R. van Gastel, I. Sikharulidze, S. Schramm, J.P. Abrahams, B. Poelsema, R.M. Tromp, S.J. van der Molen, Medipix 2 detector applied to low energy electron microscopy, Ultramicroscopy 110 (2009) 33–35.
[52] I. Sikharulidze, R. van Gastel, S. Schramm, J.P. Abrahams, B. Poelsema, R.M. Tromp, S.J. van der Molen, Low energy electron microscopy imaging using Medipix2 detector, Nuclear Instruments and Methods in Physics Research Section A: Accelerators, Spectrometers, Detectors and Associated Equipment 633 (Suppl. 1) (2011) S239–S242.
[53] G. Zanella, R. Zannoni, The detective quantum efficiency of an imaging detector, Nuclear Instruments and Methods in Physics Research Section A: Accelerators, Spectrometers, Detectors and Associated Equipment 359 (1995) 474–477.